SF2A 2016
C. Reylé, J. Richard, L. Cambrésy, M. Deleuil, E. Pécontal, L. Tresse and I. Vauglin (eds)

THE GASEOUS PROTO-CLUSTER: BETTER CHARACTERIZING THE INITIAL CONDITIONS OF STELLAR CLUSTER FORMATION?

Y.-N. Lee[1] and P. Hennebelle[1,2]

Abstract. Cluster formation simulations have always been numerically challenging due to the large range of spatial and temporal scales that vary by orders of magnitudes and multiple physical mechanisms involved. The simulation box is typically of parsec (pc) scale while resolution down to a few astronomical units (AUs) is needed to well resolve individual stars. However, studies of this kind are important for the understanding of the interaction between gravity and turbulence that guides the star formation and the mechanisms through which the possibly self-regulated initial mass function (IMF) is shaped by stellar feedback. Most simulation works have initial conditions that correspond to molecular clouds (MCs), while the actual star formation occurs in a very small volume fraction of the whole simulation box. We present a series of simulations to characterise the early stage of cluster formation, of which a primary stage of gas concentration is noticed. We denote this stage as the gaseous proto-cluster, which forms from gravo-turbulent collapse of the MC. This high-density region is indeed the principle site of star formation. The existence of this primary stage implies that the cluster formation environment is somewhat universal and cluster formation studies could therefore set out from more local conditions, therefore reducing the computational demand.

Keywords: ISM, turbulence, gravity, cluster formation

1 Introduction

Stars are the building blocks of the Universe. Assembled, they form associations, clusters, and galaxies. Individually, they harbour planetary systems which can eventually breed living being. Due to the hierarchical nature of astronomical structures. Star formation is complex in such a way that large scales and small scales are inter-connected and both play important roles. Galactic dynamics at scales up to a few kilo-parsec (kpc) create molecular clouds (MCs) through shearing or turbulent movements. Pre-stellar cores (10s of astronomical units) form within MCs and eventually form stars. During and at the end of their lives, stars inject energy and materials back into the environment through various feedback mechanisms including the proto-stellar jet, ionising radiation, stellar wind, and super novae.

In terms of numerical simulation, the computational box must be large enough so that the large-scale dynamic is not neglected and that the small-scale dynamics can be generated self-consistently. Meanwhile, this guarantees that the boundary condition should not have a strong artificial impact on the results. In the context of stellar cluster formation, this often leads us to a setup with a MC, or part of a MC (a few pcs) containing at least 100 solar masses ($M_\odot$), or sometimes up to a few thousands. As to correctly follow the cluster formation, at least the star-forming core scale (10s of AU or 10^{-4} pc) has to be resolved. The resolution of this kind of simulations, therefore, needs to be very high (equivalent 2^{13-15} cells in each dimension on a cartesian grid). On the other hand, different forms of energy such as the thermal motion, turbulence, magnetic field, radiation, and cosmic rays all have similar strength of ~ 1 eV cm^{-3}. The interactions amongst them are therefore important. Considering all these, a simulation of cluster formation is extremely expensive if we want to accurately follow all the physics. At the same time, it means that it is difficult for us to isolate individual problems and study them in a simplified setup. To reduce the complexity, the study of star formation is often decomposed into hierarchical steps. Stars are frequently observed to be born in clusters and many studies stress the importance

[1] Laboratoire AIM, Paris-Saclay, CEA/IRFU/SAp – CNRS – Université Paris Diderot, 91191 Gif-sur-Yvette Cedex, France
[2] LERMA (UMR CNRS 8112), Ecole Normale Supérieure, 75231 Paris Cedex, France

of understanding star formation in this context (Lada & Lada 2003; Longmore et al. 2014). In this study, we focus on the formation of a gaseous proto-cluster, the gas assembly phase and the beginning of star formation, with a view to better characterise the star formation environment and to prescribe more precisely the physical mechanisms at play.

Murray (2009) pointed out the relation $R \propto M^{1/3\sim1/2}$ for low-mass embedded clusters, where R and M are the gas radius and mass, with the catalog reported by Lada & Lada (2003). Adams et al. (2006) also compiled data from Lada & Lada (2003) and Carpenter (2000) and showed a number-size relation $R_* \propto N_*^{1/2}$ between the radius of the cluster and the number of objects it contains. The results of Gutermuth et al. (2009) are also compatible with this relation. The number-size relation is reasonably equivalent to the mass-size relation if we adopt a universal initial mass function (IMF) and thus similar characteristic mass among clusters. Larger data sets of star-forming clumps also exhibit a mass-size relation $R \propto M^n$ (Fall et al. 2010; Urquhart et al. 2014, $n = 0.38$ or 0.50). These results are obtained from molecular lines and dust continuum observations of the star-forming gas, suggesting that the mass-size relation and probably some other properties of the stellar cluster are established as early as the gas-dominated phase. Pfalzner et al. (2016) pointed out that the mass-size relation for embedded clusters and gaseous proto-clusters follow the same trend with a shift in absolute value, which could be explained with star formation efficiency or cluster expansion. The existence of this mass-size relation suggests that the gaseous proto-cluster is very likely in some equilibrium state governed by the MC environment in which it resides, and is crucial for understanding the nature of the cluster and, more generally, star formation. We emphasise here a global equilibrium, which does not imply that the structure is not locally collapsing.

Many numerical studies of star or core formation inside MCs have been performed to understand the impact of turbulence and gravity on star formation and the origin of the IMF (Padoan et al. 2007; Schmidt et al. 2010; Girichidis et al. 2011, 2012; Klessen et al. 1998; Klessen & Burkert 2000; Bonnell et al. 2003, 2008; Smith et al. 2009; Ballesteros-Paredes et al. 2015). In this study, we focus on understanding the gas-dominated phase of early cluster formation inside MCs, and show the properties of the gaseous proto-cluster are determined by those of its parent MC and are subsequently inherited by the stellar cluster. We focus on the transition between the global collapse at larger scales and the energy equilibrium that is reached for this gas-dominated object through gravo-turbulent interaction. The dense proto-cluster provides a favorable environment for star formation, and certain characteristics of the stellar cluster are therefore determined at the gas-dominated phase. In order to characterise the gaseous proto-cluster formed in MCs collapsing under self-gravity, we perform a series of simulations of gaseous proto-cluster formation inside a MC with various levels of initial turbulent support. We identify such gaseous proto-cluster regions and analyse their properties to examine whether these structures are indeed objects in equilibrium and if they coincide with observations of star-forming clumps. We also discuss the sink particles forming therein and compare the sink cluster with observations of embedded clusters. Once the nature of the clusters is known, we can investigate star formation given this recipe of a cluster environment to gain knowledge of the star formation rate, the star-forming mechanisms, the IMF, etc. From a numerical point of view, the wide range of temporal and spatial scales concerned in star formation simulations have always been computationally challenging. The knowledge of how a gaseous proto-cluster forms in a MC could serve as a valuable tool for initialising a more realistic star formation simulation without having to include the whole cloud into the simulation box, and thus could help gaining computation time or resolution.

2 Simulations: self-gravitating molecular cloud

We perform numerical simulations of a collapsing MC under self-gravity with the magneto-hydrodynamic (MHD) adaptive mesh refinement (AMR) code RAMSES (Teyssier 2002; Fromang et al. 2006). The evolution of the cloud is governed by ideal MHD equations with a cooling function of the interstellar medium (ISM) considered, as that described by Audit & Hennebelle (2005). A series of MCs with different levels of initial turbulence is simulated. Simulations are initialised with a Bonnor-Ebert-like spherical cloud of 10^4 $M_\odot$ that has a density profile $\rho(r) = \rho_0 / \left[1 + \left(\frac{r}{r_0}\right)^2\right]$ with ten times density contrast between the center and the edge, where $\rho_0 = 822$ cm^{-3} and $r_0 = 2.5$ pc. The cloud has 15 pc diameter and the computational box is twice the size of the cloud. The space surrounding the cloud is patched with diffuse gas of uniform density $\rho_0/100$. The initial temperature is set by the cooling function and it is about 10 K in the dense gas. A turbulent velocity field is generated with a Kolmogorov spectrum with random phase and is scaled in such a way that the initial Mach numbers are 2.7, 6, 7.3, and 10, respectively. A weak magnetic field with uniform mass-to-flux ratio in the x

Table 1: Simulation parameters: the cloud is specified with varying level of the ratio $t_{\rm ff}/t_{\rm vct}$. We list corresponding turbulent velocity and virial parameter $\alpha_{\rm vir} = 2E_{\rm kin}/E_{\rm grav}$.

Label	$t_{\rm ff}/t_{\rm vct}$	$v_{\rm rms}$ (km/s)	Mach	$\alpha_{\rm vir}$
A	0.4	0.6	2.7	0.12
B	0.9	1.5	6.0	0.64
C	1.1	1.8	7.3	0.96
D	1.5	2.4	10	1.78

direction is applied. Its highest value is about 8 μG at the cloud center. The ratios of characteristic timescales at the central plateau region ($r < r_0$) are used as parameters to specify the initial conditions. The ratio of free-fall time to sound crossing time $t_{\rm ff}/t_{\rm sct} = 0.15$ and the ratio of free-fall time to Alfvén crossing time $t_{\rm ff}/t_{\rm act} = 0.2$, which corresponds to mass-to-flux over critical mass-to-flux ratio of 8, are fixed for all runs. Both thermal and magnetic energy are small compared to the gravitational potential energy. The ratio between free-fall time and turbulent crossing time $t_{\rm ff}/t_{\rm vct}$ is varied in each run, giving different levels of kinetic support against self-gravity. In Table 1, we provide the values of $t_{\rm ff}/t_{\rm vct}$ and the corresponding turbulent rms velocity, Mach number, and virial parameter $\alpha_{\rm vir} = 2E_{\rm kin}/E_{\rm grav}$ to characterise the initial energy state of the MC.

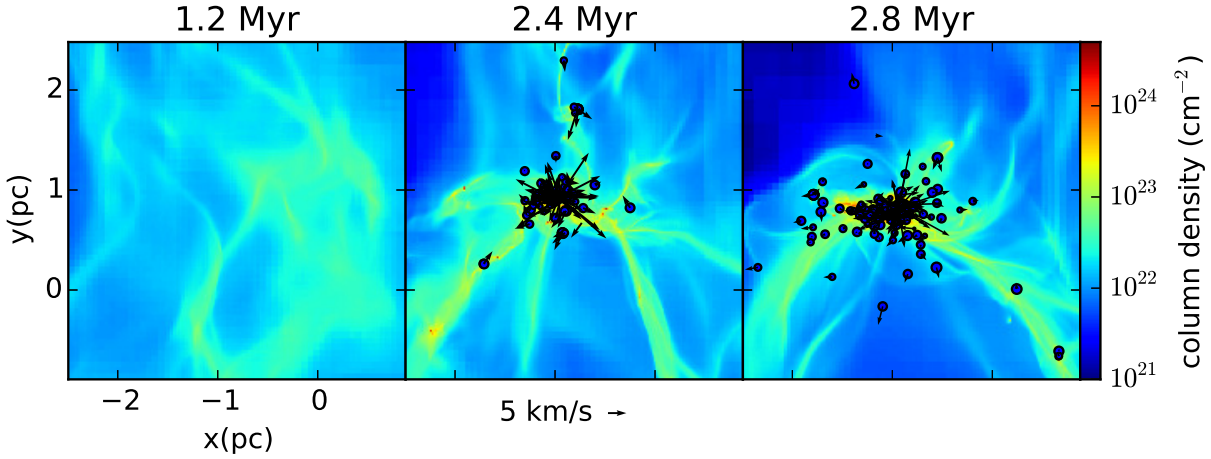

Fig. 1: Zoomed images of run B at times 1.2, 2.4, and 2.8 Myr. Sink particles over-plotted on column density. The circles represent the sink particles with the size proportional to the log of their masses and the arrows indicate their velocity. The origin of corresponds to the center of the simulation box.

We start with a 128^3 base grid and allow seven levels of refinement (equivalent to 16384^3) using an AMR scheme to ensure that the Jean's length is always resolve by 10 cells. This corresponds to resolution of 0.23 pc on the coarse grids and 0.002 pc (or 400 AU) at the densest regions. Neumann boundary conditions with imposed zero gradients are used, which allows the gas to outflow freely. Sink particles (Bleuler & Teyssier 2014) are used in our simulations, and the densest region unresolved with a fluid description is replaced with a sink particle to economise computational power and to follow accretion onto Lagrangian mass. These particles are formed when density exceeds 10^8 cm^{-3}, while the flow is convergent and gravitationally bound. After their formation, the sink particles continue to accrete mass from their surrounding. As these high density regions represent possible star formation sites, they furnish dynamical and statistical hints on stellar cluster properties. We caution that although our resolution is very small with respect to the cluster size, ensuring good description of the cluster itself, the sink particle size is too large for the sinks to represent individual stars. The typical mass of our sink particles is on the order of $\simeq 10$ M$_\odot$.

Figures 1 and 2 show zoomed views of the central region of run B where the proto-cluster is forming in column density with sink particles and in density sliced map with velocity over-plotted from two angles of view. The cloud is globally collapsing, while filamentary structures are forming under gravo-turbulent interactions. A pc-scale prominent entity of relatively high density emerges in the central region, and its size is slowly varying in time. A general rotational motion becomes evident as the collapse proceeds, since there is no dissipative mechanism at this scale strong enough to remove large amount of angular momentum. The global infalling

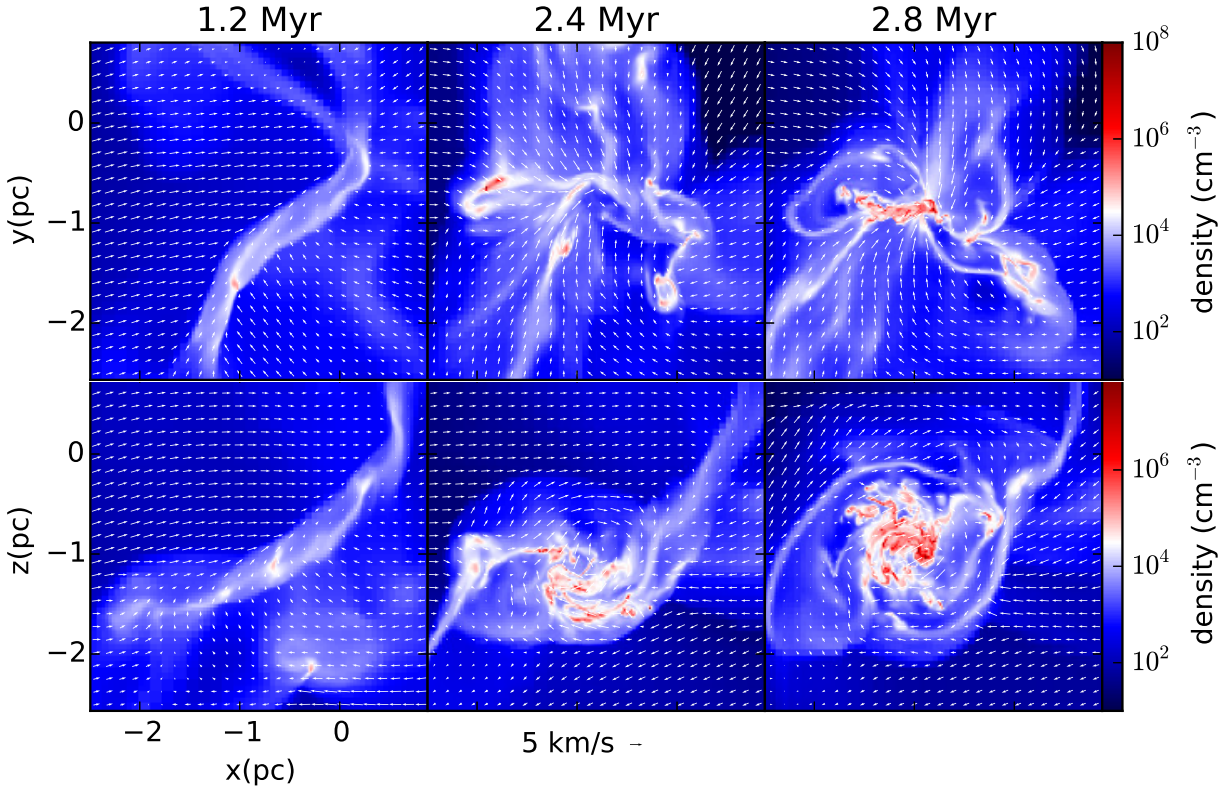

Fig. 2: Zoomed images of run B at times 1.2, 2.4, and 2.8 Myr focusing on the central dense objet with two views showing the flattened shape. **Top:** velocity field overplotted on density sliced map of the flattened rotating proto-cluster, edge-on view. **Bottom:** same as top, face-on view .

motion is noticeably reduced upon striking the central objet, forming highly irregular shocks at the seemingly ill-defined border. For the first stage of this work, simple scenario without stellar feedback is employed, in which nothing except the depletion of cloud gas can stop sink accretion. We therefore stop the simulations when about half of the initial cloud mass has been accreted onto the sink particles, since the results are less likely to be physical in this stage. This corresponds to physical time of about three million years. While some of the sink particles form in the filamentary structures feeding the central cluster, most of the sinks are observed to form within the gaseous proto-cluster, hence strongly suggesting that this central region is an important site for understanding star properties such as the IMF.

3 Identifying the proto-cluster from simulation results

Using the gas dynamics to characterize the proto-cluster and the sink distribution for the embedded cluster, respectively, we develop algorithms to identify the cluster region with highly irregular border.

3.1 The gaseous proto-cluster

In the density maps shown in Fig. 2, we see a dense, flattened structure forming at the center that is dominated by rotation. The infalling motion is stopped by a shock at the border, where we see an abrupt change in flow directions. Despite the accreting mass, the size is relatively stationary. The turbulent nature of this region prevents us from studying the detailed gas behaviour, and we, therefore, calculate integrated quantities to get rid of pronounced fluctuations. We first determine a series of ellipsoids, and then decide which one best represents the cluster.

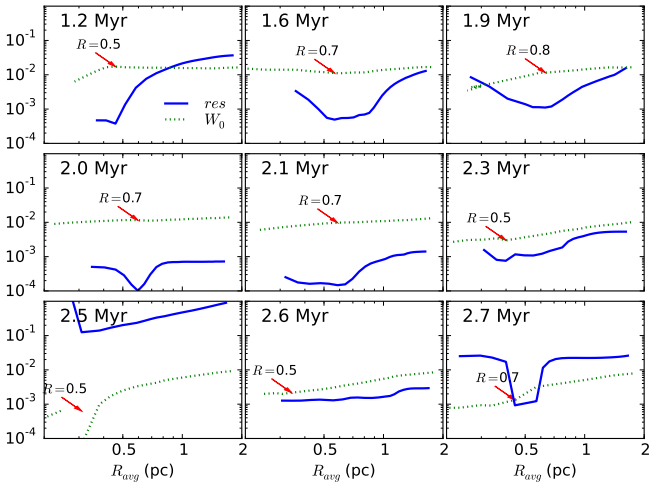

Fig. 3: Examples of the piecewise fit at nine time steps for the run with $t_{\rm ff}/t_{\rm vct}$=0.9. The normalized residual is plotted as function of cluster characteristic radius $R_{\rm avg} = (R^2H)^{\frac{1}{3}}$ in blue solid curves, of which the optimal value is such that the fit is the best. The infall moment $W_0(R_{\rm avg})$ is shown in arbitrary units with green dotted curves. The gaseous proto-cluster radius at which there exists a change in slope is indicated with a red arrow and the size of the semimajor axis is indicated.

3.1.1 Step 1: Integrated gas properties of an ellipsoid

In order to define the cluster, we calculate the center of mass, total angular momentum, and moment of inertia in an oblate ellipsoidal region of semi-major axis R and semi-minor axis H. For a series of R values, we compute iteratively to find the corresponding H by replacing *1)* the geometrical center with the center of mass, *2)* the minor axis with the axis of rotation, and *3)* the geometrical aspect ratio with that obtained from mass distribution, i.e., the inertia momenta, until convergence is reached. We find that the procedure typically converges in around ten iterations leading to a variation of less than 10^{-4} and gives reasonable results. The ellipsoids attained therefore satisfy the following criteria:

$$\vec{x}_{\rm center} = \frac{\sum \vec{x}_i m_i}{\sum m_i}, \qquad \vec{a}_H \,/\!/ \sum m_i \vec{v}_i \times \vec{r}_i, \qquad (\frac{H}{R})^2 = \frac{\lambda_1}{\sqrt{\lambda_2\lambda_3}}. \tag{3.1}$$

The quantities x and m with subscript i indicate the position and mass of each cell inside the ellipsoid; $\vec{a}_H$ is the vector representing the direction of the minor axis. The eigenvalues of the moment of inertia are $\lambda_{1,2,3}$ in increasing order. This procedure defines a series of self-consistent ellipsoids contained within each other. The disordered nature of the flow causes the ellipsoids to be not necessarily similar nor aligned.

3.1.2 Step 2: The fitting procedure

A cloud forming a central cluster features a collapsing envelope and a quasi-stationary core with minor infalling motion. To distinguish between the two, we define a quantity

$$W_0 = \int_{V(R)} \vec{v}\cdot\vec{n}\; dm \;/\; \| \int_{V(R)} \vec{v}\times\vec{n}\; dm \| \tag{3.2}$$

for the series of ellipsoids of different size to observe the change in the collapsing motion, where $\vec{v}$ is the velocity and $\vec{n}$ the unit vector pointing from the ellipsoid center to the cell position. While the envelope is expected to be globally infalling, the gaseous proto-cluster itself should be relatively stationary with more prominent rotation. The quantity W_0 thus follows different radial dependence inside and outside the proto-cluster. We propose a simple piecewise power-law description that differentiates the flow properties inside and outside the gaseous proto-cluster. As shown in Fig. 3, the infall moment exhibits a change in slope in log scale. Inside the cluster, the gas is no longer necessarily collapsing and W_0 can even change signs. A piecewise fit is performed and the residual calculated to define the semimajor axis R_* of the gaseous proto-cluster. This expression is

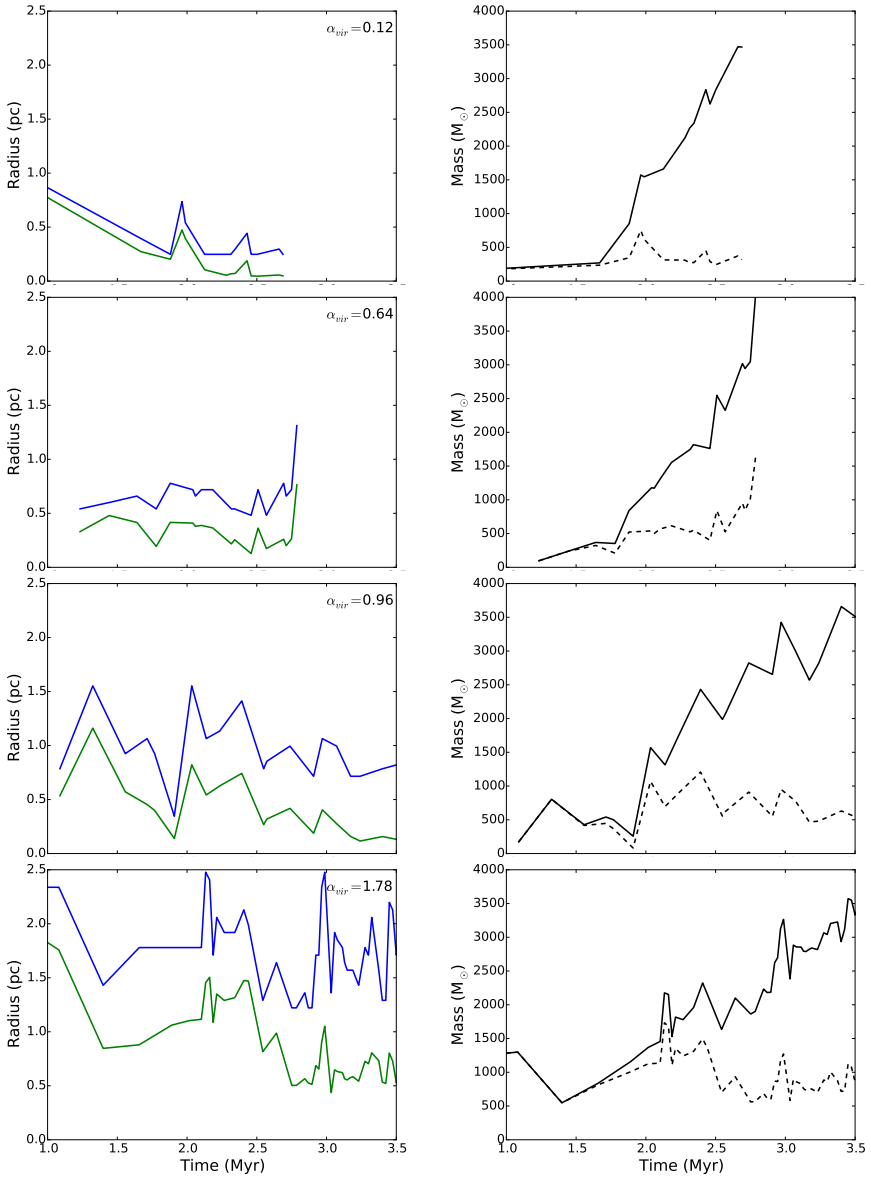

Fig. 4: **Left:** Time evolution of the semiaxes R and H of the ellipsoidal gas cluster. **Right:** Cluster mass shown as function of time. The two curves represent the gas mass (dashed) and that plus the sink mass (solid) inside the ellipsoidal region defined with gas kinematics. From top to bottom are runs A, B, C, and D with increasing levels of turbulence. The proto-cluster size increases with turbulence level. Most of the mass is accreted onto the sinks while the cluster mass increases in time, therefore the gas mass stays roughly constant.

written as

$$W_{0,\mathrm{fit}}(R_{\mathrm{avg}}, r_*) = \begin{cases} a_c R_{\mathrm{avg}}^{b_c} & \text{for} \quad R_{\mathrm{avg}} < r_* \\ a_e R_{\mathrm{avg}}^{b_e} & \text{for} \quad R_{\mathrm{avg}} > r_* \end{cases} \tag{3.3a}$$

$$res(r_*) = \frac{1}{n_R} \sum_R \left[\frac{W_{0,\mathrm{fit}}(R_{\mathrm{avg}}, r_*) - W_0(R)}{W_0(R)} \right]^2 \tag{3.3b}$$

$$R_* = \arg\min res(r_*). \tag{3.3c}$$

The average radius of the ellipsoid $R_{\mathrm{avg}} = (R^2 H)^{\frac{1}{3}}$ is used to perform the power-law fit. Other combination of R and H are tested and the results have no strong dependence on this choice. The inner part of the fitted function is put to zero when there are fluctuations around zero, and the negative points are omitted when fitting

the outer part. The size of the gaseous proto-cluster is defined as the radius at which the minimal local minimum occurs.This normalised residual of the best fit is usually smaller than 10^{-3}, and its square root implies an error of a few percentage of the fit. The fit residual is large when there are changes in sign of W_0 as a result of our definition of the functions, but the radius is on the contrary very well defined in such cases. A local minimum of the fit residual cannot always be found. This might be because the gas is highly turbulent and that there is a fluctuating shock zone between the envelope and gaseous proto-cluster, which deteriorates the fit if it is included in either of the two domains. Nonetheless, when it exists, it marks well the transition between the two regimes. Moreover, the obtained result is in good coherence of the dense region seen from the visualisations.

The inferred evolution of the size and mass of the cluster are presented in Fig. 4. Despite its turbulent nature, the size of the gaseous proto-cluster stays relatively constant while mass is accreted. The more turbulent the initial cloud is, the larger the proto-cluster is. The mass evolution is plotted with the gas mass and total mass (sinks inside the ellipsoid included). The gas mass stays roughly constant while the total mass increases, implying that most of the mass accreted onto the cluster ends up in the sinks. As expected, the radius drops with $\alpha_{\rm vir}$ because of the weaker rotational and turbulent support. This is reproduced by the analytical model developed in (Lee & Hennebelle 2016b). It is important to note that these simulations are performed without stellar feedback. With feedback considered, the sink formation and accretion could be substantially delayed and/or reduced.

3.2 The embedded sink cluster

The sink particles trace the dense region, where stars formation occurs, therefore the sink particle distribution is representative of the stellar cluster and can be used to infer the cluster size.This is carried out by computing the three eigenvalues of the rotational inertia matrix of sink particles with respect to their center of gravity. The eigenvalues represent not only the size but also the shape of the sink particle cluster. The rotational inertia matrix and the inferred radii are

$$I_{\rm rot} = \sum_i m_i \begin{bmatrix} x_i^2 & x_i y_i & x_i z_i \\ x_i y_i & y_i^2 & y_i z_i \\ x_i z_i & y_i z_i & z_i^2 \end{bmatrix}, \quad \text{and} \quad r_i = \beta \sqrt{\frac{5\lambda_i}{M}},\ i = 1, 2, 3, \tag{3.4}$$

where i is the index of sink particles, M the total mass of sinks, and $\lambda_1, \lambda_2, \lambda_3$ three eigenvalues of $I_{\rm rot}$. The factor 5 comes from the uniform mass distribution assumption, and a correctional factor $\beta \geq 1$ accounts for the fact that the mass might be centrally concentrated. From a first calculation (see dashed lines in Fig. 5), it is clear that the sink particles are very extendedly distributed, and that the concentration in certain directions gives a relative large eigenvalue compared to the other two. However, sinks forming inside the filaments feeding the cluster or those ejected by N-body interactions should not be taken into account when studying the cluster itself. We thus refine the calculation by omitting the sink particles that have larger distances than the largest semi-axis from the first calculation and repeating the same procedure. We search for convergence by increasing β starting from unity. We employ the smallest β value that yields convergence, which is always between 1 and 1.5. The convergence is reached in a couple of iterations. This yields a cluster which is more spherical and stays roughly constant in size as the total sink mass increases. The evolution of the sink cluster radius and mass are plotted in Fig. 5. The total mass of all sinks is plotted in dotted curves while that of those inside the cluster is plotted with dashed curves. The total mass including the gas is also plotted in solid curves. The selection of clustered sinks is not always robust, and the inferred size shows spiky fluctuations despite the generally stable trend it exhibits. However, the significantly reduced size and relatively mild decrease in mass suggest that the distant sinks,which make up only a small fraction of the mass, are effectively rejected.

3.3 The cluster mass-size relation

The mass-size relation is one of the important characteristics of proto-clusters that can be compared with observations. On the left of Fig. 6, the mass-size relations of gaseous proto-clusters defined with gas kinematics are over-plotted with observations of star-forming clumps (Fall et al. 2010; Urquhart et al. 2014), and the number-size relations of clusters obtained from sink distributions are over-plotted with embedded cluster observations (Adams et al. 2006; Gutermuth et al. 2009). Early time steps (before 2 Myr) are plotted with thinner lines. As the gaseous proto-cluster accretes mass, it arrives on the observed sequence. The larger the turbulence in the parent cloud, the more expanded the proto-cluster since the mass feeding the proto-cluster has higher kinetic energy and the rotation is also more important. For the sake of comparison with observations, we also show the

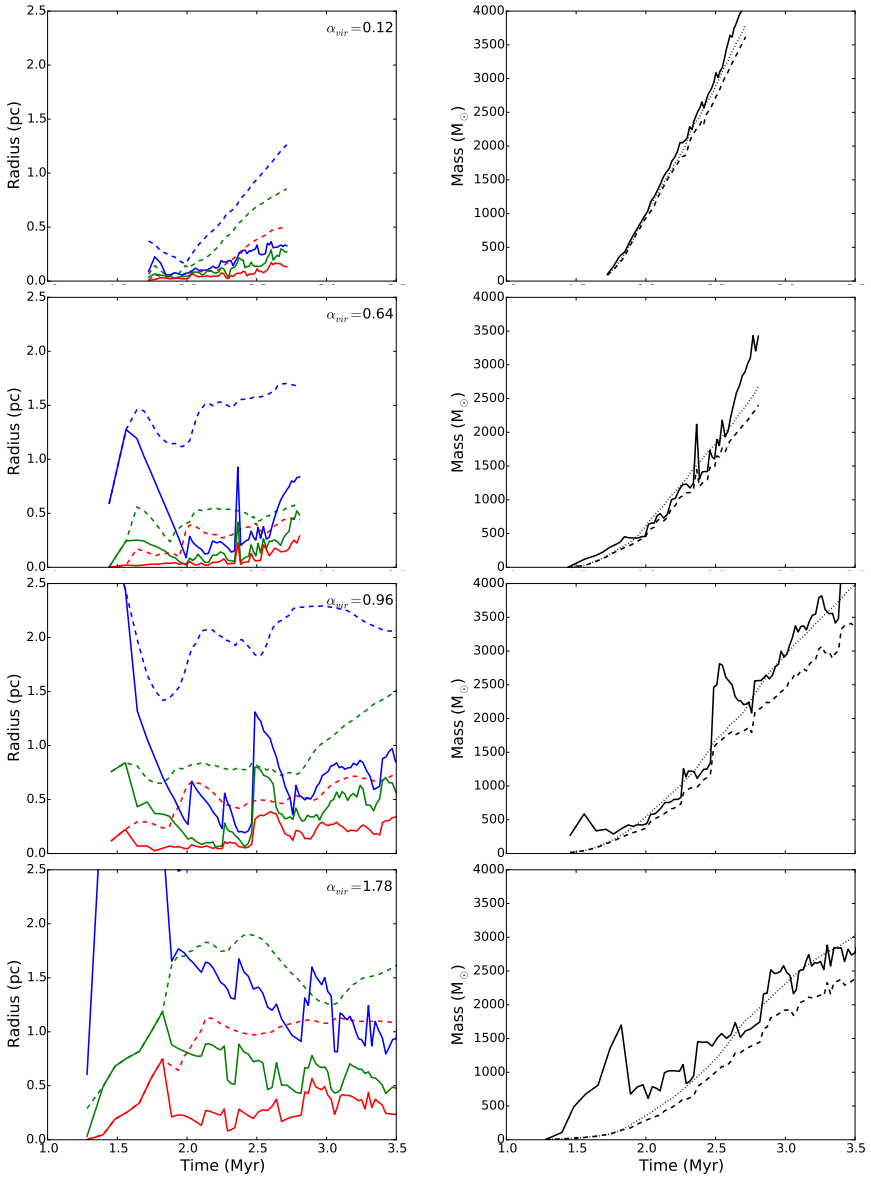

Fig. 5: **Left:** Time evolution of the three semi-axes of the cluster determined with sink particles. The dashed curves and solid curves represent the values calculated with all sinks and the reduced values with distant sinks omitted, respectively. **Right:** Sink mass (dashed) and total mass (solid) inside cluster region defined with sink distributions plotted against time. The dotted line represents the sink mass before sink removal. Removing the sink particles far away from the center drastically reduces the size while only mildly decreasing the total mass. From top to bottom are runs A, B, C, and D with increasing levels of turbulence.

relation obtained by Adams et al. (2006) R (pc) $\propto (N/300)^{1/2}$. The sink clusters come close to this sequence after sufficient evolution. At a later stage, they form fewer new sinks and start increasing in radius. Further discussion is needed, however, as our sinks are massive and do not represent individual stars. The number-size (or mass-size) relation inferred with sink particles is thus biased and not exactly representative of the embedded cluster itself. Observationally speaking, Pfalzner et al. (2016) plotted the number-size relation for different star-forming regions and found that, even though this relation follows the same trend inside different regions, its absolute value in number can vary by a factor 20 (their Fig. 3). The cluster definition and distance of the object could play important roles. On the other hand, we see that the sink cluster radius does not change very much with time, at least implying that at the early stage of cluster formation, the stars should still somewhat be correlated to and regulated by their natal gas. If we assume a 0.5 M$_\odot$ averaged mass for the stars inside

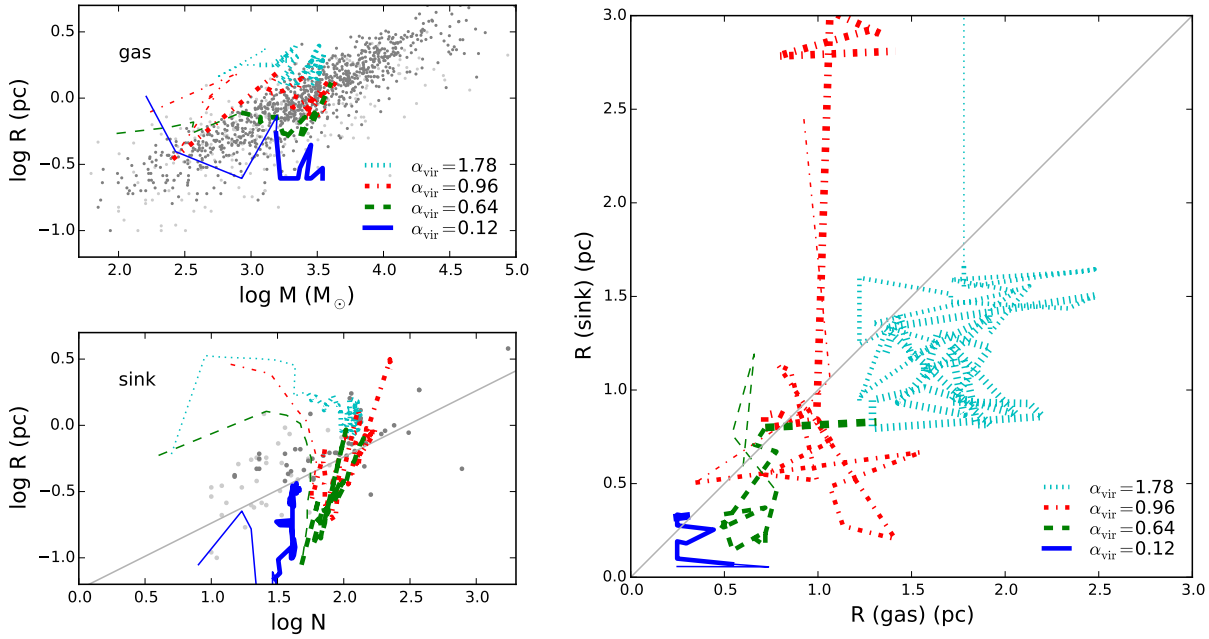

Fig. 6: **Left top:** Gaseous proto-cluster mass-size relation defined with gas kinematics over-plotted with measurements of star-forming clumps (Fall et al. 2010; Urquhart et al. 2014). The total mass of the cluster is used (gas plus sinks). **Left bottom:** Sink cluster number-size relation over-plotted with embedded cluster (Adams et al. 2006; Gutermuth et al. 2009). The gray line indicates the number-size relation R (pc) $\propto (N/300)^{1/2}$ (Adams et al. 2006). Simulations with four different levels of turbulent support are plotted. The blue solid, green dashed, red dot-dashed, and cyan dotted curves have virial parameters $\alpha_{\rm vir}$ = 0.12, 0.64, 0.96, 1.78, respectively. The curves represent the time sequence. As the proto-clusters accrete, they gain in mass and move from left to right in the figure. Time steps before 2 Myr are plotted with thinner lines. **Right:** Radius of sink clusters plotted against radius of gas proto-clusters for four runs. The relations are plotted with thinner lines for time before 2 Myr and with thicker lines after 3 Myr. The gas and sink cluster sizes show good correlation in general, while the sink cluster size is slightly smaller than that of the gas cluster.

the clusters, a star formation efficiency of less than 10% is required to reconcile the two relations given that the cluster size does not evolve. Alternatively, this could also be explained by an expansion after the cluster formation. We inferred the cluster size for gas and sinks, which enables a comparison between the two and allows us to compare the cluster size with observations as well. We stress that according to our analysis, the link between the gaseous proto-cluster radius and that of the embedded cluster is not a trivial matter. Therefore, the 20% efficiency that is usually inferred should be regarded with great care.

We compare the cluster size inferred with gas and sinks in the right panel of Fig. 6. The sink clusters generally are smaller in size than the gas clusters. This implies that the stars are formed in the inner region of the gaseous proto-cluster. The relations are plotted with a line thickness that increases with time. We can see in both the green and red curves that at early time the sink cluster radius is large probably due to the bad definition of a cluster with very few sinks. Once the cluster becomes steadily established (after 2 Myr), they show a radius that is smaller than the gaseous proto-cluster size. At an even later time (after 3 Myr with the thickest lines), the sink cluster radius shows a growth with respect to the gas radius. This might be a sign of the dynamical decoupling and expansion of the stellar cluster. Longmore et al. (2014) concluded that the gas-star coevolution cannot continue over a dynamical time, on the one hand, because the gas is dissipative while stars are ballistic and, on the other hand, because stars form from gravitational collapse of gas and create a local, gas-free environment for themselves. Parker & Dale (2015) perform a Q-parameter analysis (Cartwright & Whitworth 2004) of gas and stars in simulations and suggest that their spatial distributions are not trivially linked. This sheds light on the importance of correctly following both gas and particle dynamics in simulations and the necessity of pertinent theories of early stellar cluster formation.

To conclude, our simulations successfully reproduce the mass-size regions that we define as gaseous proto-clusters. When the cloud is too weakly supported (small $\alpha_{\rm vir}$), the gaseous proto-cluster is strongly accreting

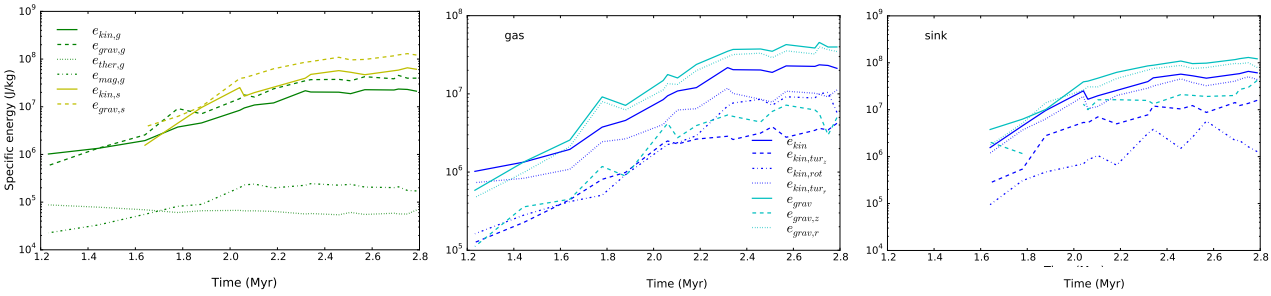

Fig. 7: **Left:** different forms of specific energy of the cluster defined with gas kinematics plotted against time. The gas component is plotted in green and the sinks are plotted in yellow. The solid, dashed, dotted, and dash-dotted lines represent kinetic, gravitational, thermal, and magnetic energies respectively. The gravitational energy is plotted in absolute value. **Middle and Right:** kinetic (blue) and gravitational energy (cyan) decomposition of the gas component (middle panel) and the sink component (bottom panel) of the proto-cluster plotted in specific values. Total energy, energy along z-axis, rotational energy, and energy perpendicular to z-axis are plotted with solid lines, dashed lines, dash-dotted lines, and dotted lines respectively.

and has a small radius and this should probably not be compared to the observations. For other runs of clouds with $\alpha_{\rm vir}$ close to unity, a good agreement of the mass-size relation between observations and simulations is reached. As gaseous proto-clusters accrete mass, they arrive on the observed sequence, which very likely implies a stationary and quasi-equilibrium state. Although we have performed simulations of 10^4 $M_\odot$ clouds, giving gaseous proto-clusters of a few thousands $M_\odot$, the gas is almost isothermal and the results could then be rescaled to the observed mass range. The simulations are parametrised by the following two non-dimensional numbers:

$$\alpha_{\rm vir} \propto \frac{\sigma^2 R}{M} \quad \text{and} \quad \mathcal{M} = \frac{\sigma}{c_{\rm s}}. \tag{3.5}$$

If we rescale the MC in the simulation to different mass, size, and temperature such that

$$M' = AM \quad , \quad R' = A^{\frac{1}{3-\gamma}} R \quad \text{and} \quad c_{\rm s}' = A^{\frac{2-\gamma}{6-2\gamma}} c_{\rm s}, \tag{3.6}$$

where $\gamma = 1$ or 0.7 is the exponent in the Larson relation $\rho \propto R^{-\gamma}$ (Larson 1981; Falgarone et al. 2004, 2009; Hennebelle & Falgarone 2012; Lombardi et al. 2010) and A is a scaling factor. With this rescaling, $\alpha_{\rm vir}$ and $\mathcal{M}$ stay unchanged, and the new MC also follows the Larson relation. The gaseous proto-cluster inside the cloud is therefore rescaled, following $R_* \propto M_*^{\frac{1}{3-\gamma}} \sim M_*^{0.5}$. This implies that given parent clouds that follow Larson relations, the gaseous proto-clusters formed therein follow relation reported by Fall et al. (2010) and Urquhart et al. (2014). We also develop an analytical model to predict the mass-size relation of gaseous proto-clusters (Lee & Hennebelle 2016b). As long as the condition that stellar feedback is not very important stays valid, our simulations and analytical model match the observations.

4 Properties of the proto-cluster and prospectives

The goal of this study is to well characterise the star-forming gas. Having identified the cluster from simulations, we perform some analysis of their internal properties.

4.1 Energy equilibrium

Once the proto-cluster is identified, we calculate the energies in different forms inside this region and examine the balance. Since we are discussing the gas-dominated early phase of cluster formation, we use the proto-clusters previously defined with gas kinematics, which indeed show good correspondence with observations. The specific kinetic, gravitational, thermal, and magnetic energies are plotted at several time steps in the left panel of Fig. 7 for the run with $t_{\rm ff}/t_{\rm vct} = 0.9$. The gravitational energy is plotted in absolute value. For the gas component (green), the thermal and magnetic energies are a few percent of the gravitational energy, which is consistent with that initialised in the parent cloud and, therefore, do not contribute much to supporting against self-gravity at

the cluster scale. The specific thermal energy stays roughly constant and decreases mildly, indicating a slight temperature decrease due to density increase. The specific magnetic energy increases slightly as a result of magnetic flux concentration. On the other hand, the kinetic energy, which has contributions from turbulence and rotation, acts largely to support against gravitational contraction. The cluster satisfies $2E_{\rm kin,g}+E_{\rm grav,g}\approx 0$, indicating the gas component is in virial equilibrium during mass accretion. The particle component (yellow), on the other hand, begins to have higher specific kinetic and gravitational energies a short while after the sinks start forming. This implies that the sink particles are more centrally concentrated than the gas and lie in a deeper potential well, which is consistent with our previous finding that the radius determined with sinks is smaller (Fig. 6 right). This is compatible with the discovery by Bate et al. (2003) that the stars have velocity dispersion that is three times higher than that of the gas. It is remarkable that the sinks are bound almost at virial and also satisfy the relation $2E_{\rm kin,s}+E_{\rm grav,s}\approx 0$, indicating that the cluster energy properties are largely inherited from its natal gas and are determined at the early formation stage. Walker et al. (2016) suggested that clusters very likely form in a conveyor-belt mode, in which the core of the star-forming cloud accumulates mass at the same time as stars form. This is perfectly in coherence with our simulation results that stars form in the dense, gaseous proto-cluster, of which the mass and energy is sustained by accretion.

4.2 Rotation and turbulence anisotropy

The rotation makes up an important proportion of the kinetic energy of the proto-cluster and a flattened form is thus a natural consequence. We estimate the rotational energy of the proto-cluster and separate it from its turbulent counterpart. This allows us to compare the proportions of rotational and turbulent energies and also examine whether turbulence is isotropic. The rotational energy is estimated as $E_{\rm kin,rot}=\frac{1}{2}JI^{-1}J$, where J is the angular momentum the cluster, and I is its rotational inertia matrix. This allows us to eliminate turbulence by summing up various motions. Uncertainties remain, in particular, since we do not take into account the differential rotation, this is probably an underestimation. The one-dimensional turbulent energy along the rotational axis of the cluster $E_{{\rm kin},z}$ is also calculated. The turbulent energy perpendicular to the rotational axis could be thus estimated as $E_{{\rm kin},r}=E_{\rm kin}-E_{\rm kin,rot}-E_{{\rm kin},z}$. We display the energies for the run with $t_{\rm ff}/t_{\rm vct}=0.9$. In the middle panel of Fig. 7, we plot the total kinetic energy, rotational energy, turbulence parallel and perpendicular to the rotational axis, respectively, for the gas component in blue. The proportion of rotational energy increases as the gaseous proto-cluster accretes, while that of $E_{{\rm kin},z}$ is slightly decreasing. The rotational energy grows to become comparable to the turbulent energy in the same plane and makes up nearly a third of the total kinetic energy. The turbulence shows anisotropy since $E_{{\rm kin},r}/E_{{\rm kin},z}>2$, although there remain uncertainties in the estimation of the rotation. The rotation flattens the proto-cluster and this anisotropy in geometry thus makes the kinetic energy distribution anisotropic in turn. We also plot in cyan the gravitational energy of the cluster ($E_{\rm grav}$).The gravitational energy is calculated by integrating the inner product of the gravity and the position vector with respect to cluster center over the cluster volume (as is carried out in the virial theorem). With this definition, we can separate the gravitational energy into two contributions by calculating respectively with the gravitational acceleration parallel ($E_{{\rm grav},z}$) and perpendicular ($E_{{\rm grav},r}$) to the cluster minor axis. This points out the fact that not only the proto-cluster is generally in virial equilibrium, but it also satisfies a modified virial theorem that accounts for the two dimensions, i.e., $2E_{{\rm kin},z}+E_{{\rm grav},z}\approx 0$ and $2E_{{\rm kin},r}+2E_{\rm kin,rot}+E_{{\rm grav},r}\approx 0$. This motivates the decomposition of the virial theorem into two dimensions in the analytical model by Lee & Hennebelle (2016b). The right panel of Fig. 7 shows the same plot as that in the middle for the sink component of the proto-cluster. The sink particles show similar trends to the gas in general. A very different behaviour is that the rotational energy calculated for the whole system is not increasing like that of the gas. Moreover, $E_{\rm kin,rot}\ll E_{\rm kin}$, indicating that the stars are giving angular momentum to the gas and there is less a general rotation.

4.3 Density PDF

The star formation is a result of collapse induced by local over-density, therefore, essential information is imprinted in the density probability density function (PDF) of the star-forming environment, which is in turn a result of interaction between turbulence and gravity. The density PDF is important for theoretical prediction of the IMF (Padoan & Nordlund 2002; Hennebelle & Chabrier 2008, 2009; Hopkins 2012). We plot the volume-weighted density PDFs of the gaseous proto-clusters identified in the previous section and that of the parent MC in Fig. 8, and show that there are indeed fundamental differences. At the beginning of the simulation, the PDF is very close to a log-normal distribution, which is a natural consequence of the turbulence, while the gravity

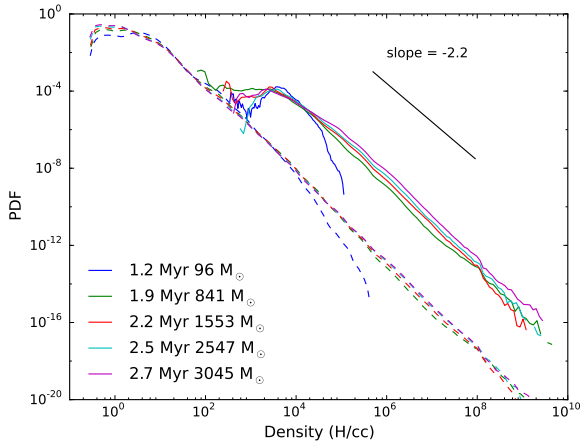

Fig. 8: In solid curves for the gaseous proto-cluster and in dashed curves for the parent cloud, the PDF at several time steps for run B with $t_{\rm ff}/t_{\rm vat} = 0.9$. The normalisation is performed such that the integral is equal to one. The distribution is close to lognormal at the beginning as a result of turbulence interaction. The gravity soon dominates and creates a prominent power-law tail. The slope -2.2 is the average of the cluster PDF slopes evaluated at the same density range as the black line except for the first time step.

soon dominates. The gaseous proto-cluster shows the same power-law high-mass tail as the parent MC with slope -2.2, which is a signature of local gravitational collapse. This is a common feature of star-forming region as first mentioned observationally by Kainulainen et al. (2009). The major difference lies in that the gaseous proto-cluster region is denser than the original cloud environment with a density peak around 10^4 cm^{-3}. The density PDF of the MC stays almost unchanged while a gaseous proto-cluster develops within. This emphasises the fact that when the stars form, their environment is already not the same as the MC in which they reside. The gaseous proto-cluster stage, of which the gas properties are modified by the interaction of gravity and turbulence, should therefore be taken into account when linking the MC to the stellar cluster.

4.4 Stellar feedback

To have a fully physical description of a realistic self-regulation of star mass accretion and cluster formation, stellar feedbacks such as radiations (Bate 2009; Price & Bate 2009; Commerçon et al. 2011; Bate 2012; Krumholz et al. 2012), protostellar jets and outflows (Wang et al. 2010; Nakamura & Li 2011, 2014; Federrath et al. 2014; Federrath 2015; Dale et al. 2013c, 2015), HII regions (Krumholz et al. 2007; Peters et al. 2010; Dale et al. 2013a,b, 2015), and supernovae (Iffrig & Hennebelle 2015; Walch & Naab 2015) should be incorporated. Here we show results of gaseous proto-cluster formation in a simulation with the ionising HII region (Geen et al. 2015) in Fig. 9. The early evolution of the proto-cluster is barely influenced by stellar feedback since massive star have not yet formed and have not been exerting energy output into the ISM. In the left panel we see that at early time the cluster forms similarly to that in the simulation without feedback. At later time, the HII region heats up proto-cluster and eventually disperses all the gas available for star formation. The cluster survives from the gas expulsion and become gas free. An interesting event is also observed in this simulation that at the expansion front of the ionising wave, a secondary cluster formation is triggered. On the right panel of Fig. 9, we calculated the radius of the gaseous proto-cluster with the previously developed method, the evolution is very similar to that without feedback until that the gas starts flowing outwards and our method becomes no longer valid. A next step of this study is to include the feedback from lower mass stars such as the proto-stellar jet.

5 Conclusions

With a set of simulations of self-gravitating MCs under global collapse, we demonstrated that star do not form uniformly in MCs. Instead, they form inside gaseous proto-cluster environments, which occupy a small volume fraction of the MC. The gaseous proto-cluster forms from the quasi-static equilibrium between the turbulence-driving accretion from the global infall and the turbulence cascade that dissipates energy. The gas inside

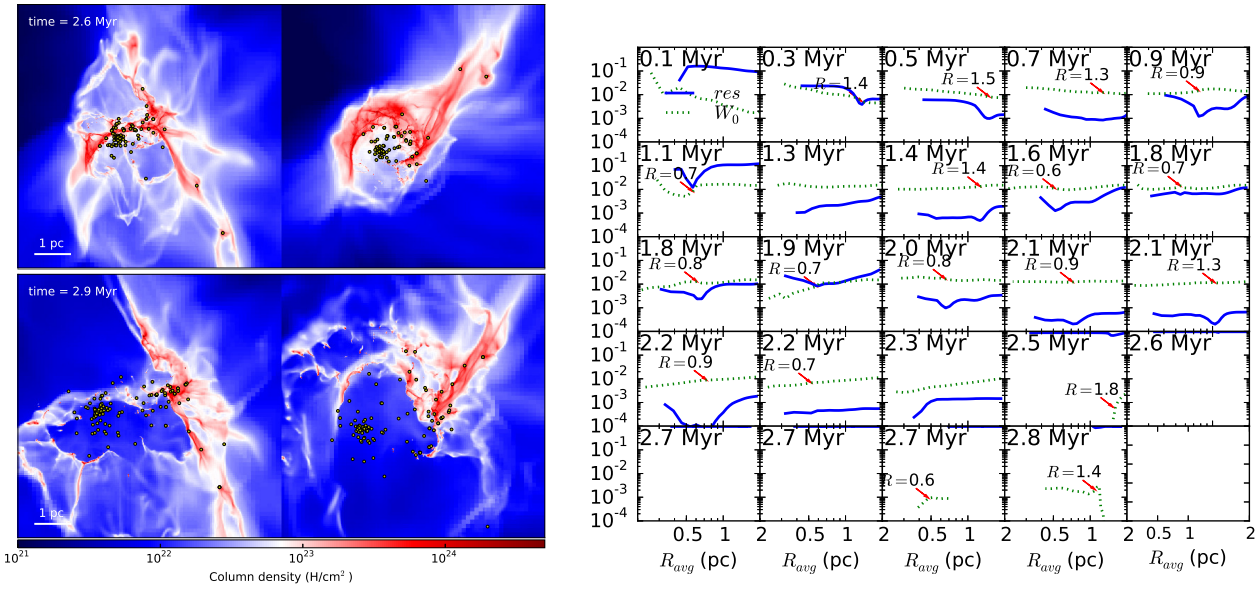

Fig. 9: **Left:** Column density of simulation with HII feedback at two time steps. Circles show the stellar cluster that survives the gas expulsion. **Right:** Radius identification of the gaseous proto-cluster at several time steps.

the gaseous proto-cluster is reprocessed and is denser, more turbulent than the averaged MC. The gaseous proto-cluster mass and size could be inferred from its parent MC and there exists a mass-size relation from observations that is reproduce with our simulations. The proto-clusters inferred with gas and sink components are compared to the observed star-forming clumps and embedded clusters, respectively. Both the gas and sink clusters show stationary behaviour in size and are coherent with observations. We stress that although the stellar cluster radius and the gaseous proto-cluster radius are correlated, their exact values are sensitive to the definition adopted. Therefore, this implies that any interpretation in terms of gas removal or efficiency should be taken with care. Energy analyses show that the proto-cluster is in virial equilibrium such that the rotation and turbulence support against self-gravity. As turbulence is driven by the accretion from the collapsing MC, a new balance is established in this emerging entity. This is obviously prescribed by the properties of the parent MC and the nature of its collapse. The initial turbulence level in the parent MC is also imprinted in that of the gaseous proto-cluster and, consequently, determines its size.

This study shows that stellar clusters from very likely inside an environment that has universal properties and is to some extent disentangled from the parent MC, which allows us to focus on the dense regions and possibly set up a more realistic and economic initial condition for cluster formation simulations. Last but not least, we started to include stellar feedback mechanisms, such as ionising HII (Geen et al. 2016) regions and supernova (Iffrig & Hennebelle 2015), into the simulations. These kinds of high energy processes disperse that gas inside the gaseous proto-cluster and terminates star-formation at later stages, while the conclusions from earlier studies without stellar feedback stays unchanged. We conclude that the gaseous proto-cluster is indeed an important intermediate step of stellar cluster formation from MCs, and that star formation should be studied in this context. Interested readers are invited to refer to Lee & Hennebelle (2016a) for more detailed informations.

This work was granted access to HPC resources of CINES under the allocation x2014047023 made by GENCI (Grand Equipement National de Calcul Intensif). This research has received funding from the European Research Council under the European Community's Seventh Framework Programme (FP7/2007-2013 Grant Agreement no. 306483).

References

Adams, F. C., Proszkow, E. M., Fatuzzo, M., & Myers, P. C. 2006, ApJ, 641, 504

Audit, E. & Hennebelle, P. 2005, A&A, 433, 1

Ballesteros-Paredes, J., Hartmann, L. W., Pérez-Goytia, N., & Kuznetsova, A. 2015, MNRAS, 452, 566

Bate, M. R. 2009, MNRAS, 392, 1363

Bate, M. R. 2012, MNRAS, 419, 3115
Bate, M. R., Bonnell, I. A., & Bromm, V. 2003, MNRAS, 339, 577
Bleuler, A. & Teyssier, R. 2014, MNRAS, 445, 4015
Bonnell, I. A., Bate, M. R., & Vine, S. G. 2003, MNRAS, 343, 413
Bonnell, I. A., Clark, P., & Bate, M. R. 2008, MNRAS, 389, 1556
Carpenter, J. M. 2000, AJ, 120, 3139
Cartwright, A. & Whitworth, A. P. 2004, MNRAS, 348, 589
Commerçon, B., Hennebelle, P., & Henning, T. 2011, ApJ, 742, L9
Dale, J. E., Ercolano, B., & Bonnell, I. A. 2013a, MNRAS, 431, 1062
Dale, J. E., Ercolano, B., & Bonnell, I. A. 2013b, MNRAS, 430, 234
Dale, J. E., Ercolano, B., & Bonnell, I. A. 2015, MNRAS, 451, 987
Dale, J. E., Ngoumou, J., Ercolano, B., & Bonnell, I. A. 2013c, MNRAS, 436, 3430
Falgarone, E., Hily-Blant, P., & Levrier, F. 2004, Ap&SS, 292, 89
Falgarone, E., Pety, J., & Hily-Blant, P. 2009, A&A, 507, 355
Fall, S. M., Krumholz, M. R., & Matzner, C. D. 2010, ApJ, 710, L142
Federrath, C. 2015, MNRAS, 450, 4035
Federrath, C., Schrön, M., Banerjee, R., & Klessen, R. S. 2014, ApJ, 790, 128
Fromang, S., Hennebelle, P., & Teyssier, R. 2006, A&A, 457, 371
Geen, S., Hennebelle, P., Tremblin, P., & Rosdahl, J. 2015, MNRAS, 454, 4484
Geen, S., Hennebelle, P., Tremblin, P., & Rosdahl, J. 2016, MNRAS
Girichidis, P., Federrath, C., Banerjee, R., & Klessen, R. S. 2011, MNRAS, 413, 2741
Girichidis, P., Federrath, C., Banerjee, R., & Klessen, R. S. 2012, MNRAS, 420, 613
Gutermuth, R. A., Megeath, S. T., Myers, P. C., et al. 2009, ApJS, 184, 18
Hennebelle, P. & Chabrier, G. 2008, ApJ, 684, 395
Hennebelle, P. & Chabrier, G. 2009, ApJ, 702, 1428
Hennebelle, P. & Falgarone, E. 2012, A&A Rev., 20, 55
Hopkins, P. F. 2012, MNRAS, 423, 2037
Iffrig, O. & Hennebelle, P. 2015, A&A, 576, A95
Kainulainen, J., Beuther, H., Henning, T., & Plume, R. 2009, A&A, 508, L35
Klessen, R. S. & Burkert, A. 2000, ApJS, 128, 287
Klessen, R. S., Burkert, A., & Bate, M. R. 1998, ApJ, 501, L205
Krumholz, M. R., Klein, R. I., & McKee, C. F. 2012, ApJ, 754, 71
Krumholz, M. R., Stone, J. M., & Gardiner, T. A. 2007, ApJ, 671, 518
Lada, C. J. & Lada, E. A. 2003, ARA&A, 41, 57
Larson, R. B. 1981, MNRAS, 194, 809
Lee, Y.-N. & Hennebelle, P. 2016a, A&A, 591, A30
Lee, Y.-N. & Hennebelle, P. 2016b, A&A, 591, A31
Lombardi, M., Alves, J., & Lada, C. J. 2010, A&A, 519, L7
Longmore, S. N., Kruijssen, J. M. D., Bastian, N., et al. 2014, Protostars and Planets VI, 291
Murray, N. 2009, ApJ, 691, 946
Nakamura, F. & Li, Z.-Y. 2011, ApJ, 740, 36
Nakamura, F. & Li, Z.-Y. 2014, ApJ, 783, 115
Padoan, P. & Nordlund, Å. 2002, ApJ, 576, 870
Padoan, P., Nordlund, Å., Kritsuk, A. G., Norman, M. L., & Li, P. S. 2007, ApJ, 661, 972
Parker, R. J. & Dale, J. E. 2015, MNRAS, 451, 3664
Peters, T., Banerjee, R., Klessen, R. S., et al. 2010, ApJ, 711, 1017
Pfalzner, S., Kirk, H., Sills, A., et al. 2016, A&A, 586, A68
Price, D. J. & Bate, M. R. 2009, MNRAS, 398, 33
Schmidt, W., Kern, S. A. W., Federrath, C., & Klessen, R. S. 2010, A&A, 516, A25
Smith, R. J., Clark, P. C., & Bonnell, I. A. 2009, MNRAS, 396, 830
Teyssier, R. 2002, A&A, 385, 337
Urquhart, J. S., Moore, T. J. T., Csengeri, T., et al. 2014, MNRAS, 443, 1555
Walch, S. & Naab, T. 2015, MNRAS, 451, 2757
Walker, D. L., Longmore, S. N., Bastian, N., et al. 2016, MNRAS
Wang, P., Li, Z.-Y., Abel, T., & Nakamura, F. 2010, ApJ, 709, 27